Nanoscale morphology and performance of molecular-weight-dependent poly(3-hexylthiophene)/TiO$_2$ nanorod hybrid solar cells

Ming-Chung Wu,[a] Chia-Hao Chang,[a] His-Hsing Lo,[a] Yi-Shen Lin,[a] Yun-Yue Lin,[a] Wei-Che Yen,[b] Wei-Fang Su,*[ab] Yang-Fang Chen[c] and Chun-Wei Chen*[a]

We have investigated the effect of polymer molecular weight on the morphology and performance of poly(3-hexylthiophene)/TiO$_2$ nanorod hybrid photovoltaic devices by using scanning near field optical microscopy (SNOM), atomic force microscopy (AFM) and confocal Raman microscopy. From the topography and absorption mapping images, it is found that the rod-like structure of the low molecular weight polymer hybrid film consists of a large amount of grain boundaries and has a less continuous absorption mapping image. In contrast, the larger domain structure of the high molecular weight polymer hybrid film exhibits a continuous absorption mapping image, as a result of enhanced polymer stacking and electronic delocalization. The nanoscale morphology of the hybrid samples with different molecular weights also reveals the nature of photovoltaic performance and carrier transport behavior investigated by the time-of-flight technique.

1. Introduction

Polymer solar cells have attracted a great of interest recently due to their potential application in developing low-cost, solution processable, large-area, mechanically flexible photovoltaic devices.[1–3] Due to the low dielectric constants of organic materials, the dominant photogenerated species in most conjugated polymers are neutral bound electron–hole pairs (excitons). These neutral excitons can be dissociated from Coulomb attraction by offering an energetically favorable pathway for the electron from the polymer (donor) to transfer onto an electron-accepting species (acceptor). The separated carriers (electrons or holes) are transported through the device to the electrodes without recombining with oppositely charged carriers and generate photocurrent. Because the diffusion length of excitons in a semiconducting polymer is usually shorter than 20 nm,[4–6] the electron acceptors must be intermixed with polymer at a nanometer length scale to achieve efficient charge separation. Recent developments have shown that the use of interpenetrating electron donor–acceptor heterojunctions such as polymer : fullerene,[2,3] polymer : polymer[7] and polymer : nanocrystal[1,8–10] can yield efficient photovoltaic conversions. The environmentally friendly and low-cost TiO$_2$ nanocrystal is a promising material in hybrid organic/inorganic photovoltaic device applications. Two common ways have been proposed to prepare the polymer/TiO$_2$ hybrid solar cells: (i) by blending the TiO$_2$ nanocrystals with the polymer to form the bulk heterojunction[9,10] or (ii) by infiltrating the polymer into the porous TiO$_2$ nanostructures.[11,12] Several different conjugated polymers have also been used in polymer : TiO$_2$ hybrid solar cells, such as poly [2-methoxy-5-(2'-ethylhexyloxy)-1,4-phenylenevinylene] (MEH-PPV),[13–16] MEH-PPV derivatives,[11] poly[2-methoxy-5-(3',7'-dimethyloctyloxy)-1,4-phenylenevinylene] (MDMO-PPV),[17] poly(3-hexylthiophene) (P3HT)[12] and water soluble polythiophene.[18] It is known that the device performance of polymer-based solar cells strongly depends on morphology, efficiency of charge separation and transport and interfacial contact. McGehee et al.[19,20] have used atomic force microscopy to study the morphology of P3HT thin films made with different molecular weights (MWs). They found that the mobility of P3HT increases as the MW is increased. Similar observation of the molecular-weight-dependent mobilities on the performance of polymer field effect transistors (FETs) was also reported by Neher et al.[21] Recently, Heeger et al. have also demonstrated the dependence of the morphology and photovoltaic performance on MW for devices based on P3HT/PCBM.[22] They concluded that the best performance can be achieved by using an optimum ratio between high MW and low MW components. Recently, scanning near-field optical microscopy (SNOM) has become one of the high-resolution microscopic techniques that have been used to identify the relative distribution of polymers within a blend.[23–26] SNOM is a particularly valuable analytical tool for the study of conjugated polymers[27] as many of the important processes pertinent to their applications involve the emission or absorption of photons. In this article, we report the nanoscale morphology dependence of P3HT/TiO$_2$ nanorod bulk heterojunctions with different polymer MWs by employing SNOM, atomic force microscopy (AFM), and confocal Raman microscopy. In addition, the correlation between the morphology and transport behavior for P3HT/TiO$_2$ nanorod hybrids with different MWs is also explored by time of flight (TOF) mobility measurements. Finally, the photovoltaic performances of the devices based on the hybrids with different MWs are also presented.

[a]Department of Materials Science and Engineering, National Taiwan University, Taipei, 106-17, Taiwan. E-mail: chunwei@ntu.edu.tw
[b]Institute of Polymer Science and Engineering, National Taiwan University, Taipei, 106-17, Taiwan. E-mail: suwf@ntu.edu.tw
[c]Department of Physics, National Taiwan University, Taipei, 106-17, Taiwan

This journal is © The Royal Society of Chemistry 2008

J. Mater. Chem., 2008, 18, 4097–4102 | 4097

2. Experimental

2-1. Materials preparation

P3HTs with different MWs were synthesized according to the literature with some modifications.[28] Typically, 2,5-dibromo-3-hexylthiophene (0.030 mol, 10 g) was added into a 500 mL three neck round bottom flask equipped with a 24/40 ground joint, a reflux condenser, and a magnetic stir-bar. It was purged with dry nitrogen for 15 min. 320 mL freshly distilled THF was transferred to the flask and the solution was stirred under dry nitrogen. A solution of *tert*-butylmagnesium chloride in diethyl ether (0.032 mol, 16 mL) was added *via* an airtight syringe and then heated at reflux for 1.5 h. The solution was allowed to cool to room temperature followed by the addition of Ni(dppp)Cl$_2$ and stirring at room temperature for 0.5 h. The solution was poured into methanol (500 mL). This action led to precipitation. The solid was collected in a cellulose extraction thimble and then washed with methanol in a Soxhlet apparatus. By changing the amount of Ni(dppp)Cl$_2$, P3HT samples with different MWs (9.7 kDa, 29.3 kDa, and 66.3 kDa) were obtained, representing low, medium and high MW samples respectively. The polymer was driedunder vacuum overnight and gathered as a dark purple material (60% yield). The MWs and polydispersity (PDI) values of P3HT were determined by gel permeation chromatography (GPC) on a Waters 1525 Binary HPLC Pump with polystyrene as standard and tetrahydrofuran (THF) as the solvent. The regio-specificity (RR) of P3HT was determined by the NMR spectros-copy using a Bruker AVANCE 400 spectrometer with CDCl$_3$ as solvent and tetramethylsilane as an internal standard. The growth of high aspect ratio anatase TiO$_2$ nanorods was carried out by the hydrolysis of titanium tetraisopropoxide according to the literature procedure with modifications.[29] Details and results were described in an earlier work.[15] The dimensions of TiO$_2$ nanorods were about 20–40 nm in length and 4–5 nm in diameter. TiO$_2$ nanorods dissolved in pyridine and chloroform mixed solvent (weight ratios pyridine : chloroform = 2 : 7) and P3HT in chlorobenzene were then thoroughly mixed to prepare the hybrid materials.

2-2. Experiment setup and characterization

For the optical measurement, UV-Visible absorption spectra were obtained using a Jasco V-570 UV/Vis/NIR spectropho-tometer. Scanning near-field optical microscopy (SNOM, WITec, AlphaSNOM, Germany) was performed in the trans-mission mode with a special probe, consisting of a micro-fabri-cated cantilever SNOM sensor (aperture $\sim$ 100 nm). The transmitted light was collected with a $40\times$ objective and detected with a single photon counting photomultiplier tube (PMT). The scanning images were collected using a high-resolution piezo-electric stage (PI). For each line scan, 256 data points were taken with a line scan frequency of 0.5 Hz. Confocal Raman scattering mapping measurements were conducted with a confocal micro-scope (WITec, CMR200, Germany) in the backscattering mode. Diffraction-limited confocal Raman microscopy gives a lateral spatial resolution ($\sim$300 nm) about half of the excitation wave-length (λ_{exe} = 632.8 nm). The laser beam was focused with a $100\times$ NA = 0.95 objective (Olympus, IX-70) and the laser focus beam was about 1 μm in diameter, corresponding to about 3–4 pixels in the integrated Raman image. The film thickness was determined by an α-stepper (Veeco, Dektak 6M 24383). The film morphology was observed using atomic force microscopy (AFM; Digital Instruments, Nanoscope III). For the time-of-flight (TOF) mobility measurements, thick films (several μm) were prepared by drop-casting the P3HT/TiO$_2$ nanorod hybrid solu-tions on glass substrates precoated with semi-transparent aluminium electrodes (35 nm) by thermal evaporation under a vacuum of about 10^{-6} Torr. The measured samples were then completed by thermal evaporation of thicker aluminium cath-odes ($\sim$200 nm) through a shadow mask. For the TOF transient photocurrent measurements, a thin layer of charge carriers was generated under illumination through the semi-transparent electrode using a frequency-double Nd:YAG pulsed laser (λ = 532 nm). The intensity of the incident laser power was kept small enough to avoid the accumulation of photoexcitation charges, which could alter the internal electric field. Under the applied electric field, these carriers were drifted toward the counter electrode, giving a transient photocurrent signal recorded by a digital oscilloscope (Tetronix TDS5052B). The drift mobility μ at an applied electric field E is deduced according to $\mu = d/Et_{tr}$, where d is the thickness of the film and t_{tr} is the transit time for the arrival of carriers at the collecting electrode. The carrier types (electron or hole) under study were selected by changing the polarity of the applied electric field using a Keithley 2410 source meter. The samples were mounted in a vacuum chamber under 10^{-3} Torr during measurement.

The photovoltaic devices consisting of indium–tin oxide (ITO)/poly(3,4-ethylenedioxythiophene)-poly(styrenesulfonate) (PEDOT:PSS)/P3HT:TiO$_2$ nanorod hybrid/Al electrode were fabricated using the following processes. A 60 nm thick layer of PEDOT:PSS (Aldrich) was spin-casted onto the ITO substrate at 300 rpm for 10 s and 6000 rpm for one minute, followed by baking at 120 °C for 30 min. A P3HT/TiO$_2$ nanorod hybrid thin film with a weight ratio of P3HT : TiO$_2$ = 50 : 50 was spin-casted on top of the PEDOT:PSS layer with the thickness controlled at about 120 nm. An additional layer of TiO$_2$ nanorods sandwiched between the active layer and the aluminium electrode was included to act as a hole blocking layer.[16] The Al electrode was then deposited onto the TiO$_2$ nanorod layer by thermal evaporation under vacuum at pressure around 2×10^{-6} Torr. Current–voltage measurements were obtained by using a solar simulator (Newport Inc.) with an AM 1.5 filter under an irradiation intensity of 100 mW cm^{-2}.

3. Results and discussion

Table 1 summarizes the MWs, polydispersities (PDI) and regiospecificities (RR) of the pristine P3HT samples used in this study. Fig. 1 shows the absorption spectra of P3HT/TiO$_2$ nanorod hybrid thin films (50 : 50 wt%) with different polymer MWs. A redshift in the absorption peaks is found for the hybrids

Table 1 Summary of the MWs, polydispersities (PDI) and regiospeci-ficities (RR) of P3HT samples in this study

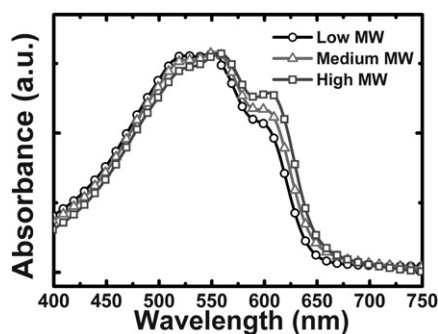| Sample of P3HT	MW/kDa	PDI	RR (%)
Low MW	9.7	1.2	>95
Medium MW	29.3	1.3	>95
High MW	66.3	1.5	>95

Fig. 1 Normalized absorption spectra of P3HT/TiO$_2$ nanorod hybrids with different molecular weights.

with increasing polymer MWs, together with more pronounced 0–0 and 0–1 vibronic absorption shoulders. The result indicates that the charge carriers and excitons in the higher MW P3HT can delocalize over a larger extent as a result of π–π stacking and
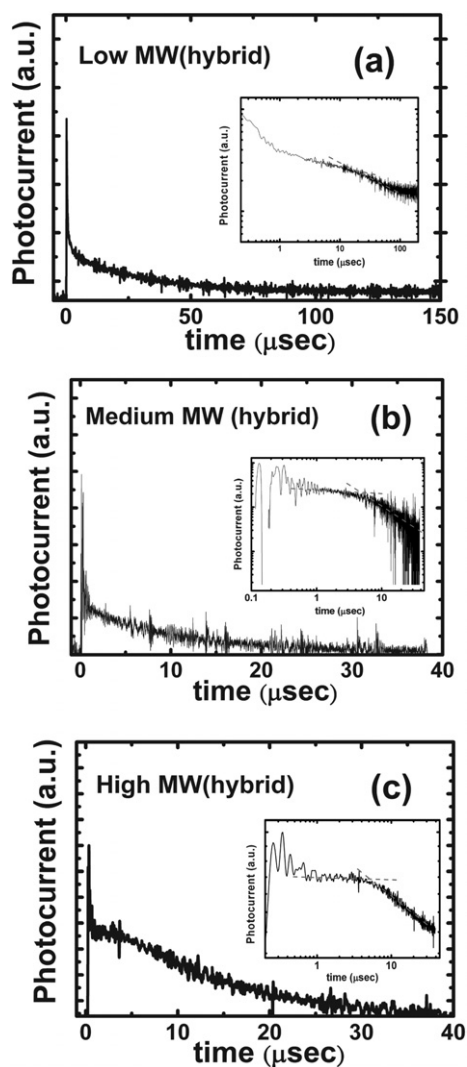

Fig. 2 The TOF hole transient photocurrents for P3HT/TiO$_2$ nanorod hybrids with (a) low, (b) medium and (c) high MWs. The insets show the double-logarithmic plots for the transient photocurrents.

a stronger wavefunction overlap. Fig. 2(a), (b) and (c) show the transient hole photocurrents for the P3HT/TiO$_2$ nanorod hybrid samples consisting of different P3HT MWs. It is found that the transient photocurrent for the low MW sample is highly dispersive and the transit time t_{tr} can be estimated from the intersection point in the double-logarithmic plot (inset) as shown in Fig. 2(a). The hole mobility for the low MW sample is about $\mu_h = 7.6 \times 10^{-4}$ cm^2 V^{-1} s^{-1} at $E = 3.0 \times 10^4$ V cm^{-1}. For the medium MW sample, the hole transient exhibits dispersive character with the mobility increased to $\mu_h = 1.8 \times 10^{-3}$ cm^2 V^{-1} s^{-1} at $E = 3.3 \times 10^4$ V cm^{-1} as shown in Fig. 2(b). For the high MW sample, the hole transient photocurrent becomes less dispersive with a clearly defined plateau region. The mobility for the high MW sample is further increased to $\mu_h = 5.0 \times 10^{-3}$ cm^2 V^{-1} s^{-1} at $E = 5.3 \times 10^4$ V cm^{-1} as shown in Fig. 2(c). The increased carrier mobility with increased polymer MW is mainly attributed to the enhanced π-electron delocalization and increased effective conjugation length in the , consistent with the previous MW dependent mobilities of pristine P3HT measured from field effect transistors or space charge limited current.[19–21]

Next, we fabricated the P3HT/TiO$_2$ nanorod hybrid photovoltaic devices by blending TiO$_2$ nanorods with different MW P3HT polymers. Fig. 3 shows the current–voltage (I–V) characteristic curves of the solar cells measured under AM 1.5 illumination. The open circuit voltages (V_{oc}), short circuit currents (I_{sc}), fill factors (FF) and the efficiencies of the solar cells (η) obtained from the I–V characteristic curves for the hybrids with different P3HT MWs are listed in Table 2. Compared to the low MW sample, the medium MW sample shows an improvement in the power conversion efficiency η, accompanied by an increase in the short circuit current density (J_{sc}) by about 80%. The increased short circuit current in the medium sample is consistent with the result of enhanced carrier mobility with MW. For the
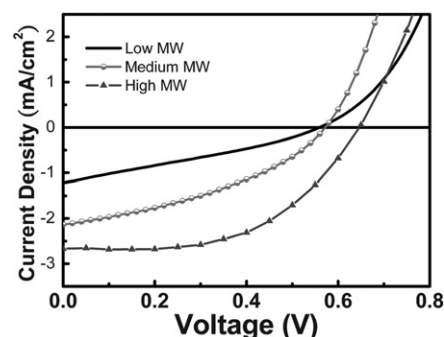

Fig. 3 I–V characteristics of the photovoltaic devices based on P3HT/TiO$_2$ nanorod hybrids with different MW P3HT (under AM 1.5 illumination (100 mW cm^{-2})).

Table 2 Performance of P3HT/TiO$_2$ nanorod hybrid solar cells under AM 1.5 illumination (100 mW cm^{-2}) for different P3HT MWs

P3HT	V_{oc}/V	I_{sc}/mA cm^2	FF (%)	Power conversion efficiency (%)
Low MW	0.55	1.22	30	0.20
Medium MW	0.57	2.14	39	0.48
High MW	0.64	2.73	56	0.98

high MW sample, large improvements in the fill factor and short circuit current are found. The improved fill factor may be attributed to the reduced serial resistance and increased carrier mobility as a result of enhanced electronic delocalization within polymer chains. In addition, the reason for the increase in V_{oc} for the high MW sample is not clear at the current stage, and one possible reason might be attributed to the reduction of back charge recombination rate at the P3HT/TiO$_2$ nanorod interfaces, which can be revealed from the nanoscale morphology in the later section. Similar device performance was also reported for the P3HT/ZnO nanoparticle hybrids,[30] where the effect of thermal annealing significantly improves the power conversion efficiency of hybrid solar cells to ∼0.9%. In this study, no thermal annealing was implemented during device fabrication. The enhancement in the P3HT/TiO$_2$ nanorod hybrid photovoltaic performance by using higher MW P3HT is mainly attributed to enhanced π-electron delocalization and more organized chain packing in the polymer, which shows good consistency with the observed redshift in the absorption spectra and increased mobilities with MWs.

Since the device performance strongly depends on the film morphology, we further carried out the investigation of the nanoscale morphology by using SNOM and AFM. In the measurements, a SNOM probe with an aperture of around 100 nm in diameter on the sharp end was placed into the near field of the investigated sample. High-quality optical contrast images were able to be obtained by this technique. In order to suppress the photoluminescence behavior of P3HT, simultaneous topography and absorption measurements were performed using a He–Ne laser of 632.8 nm wavelength. The surface topography and absorption contrast images of three P3HT/TiO$_2$ nanorod hybrid samples with different P3HT MWs are shown in Fig. 4. The low MW sample exhibits coarse surface topography (Fig. 4(a)) and discontinuous absorption mapping image (Fig. 4(b)). Due to the increased interchain stacking by increasing P3HT MW, increased smoothness in topography and more continuous absorption behavior at the corresponding region can be found with increased polymer MW as shown for the medium MW sample (Fig. 4(c) and (d)) and the high MW sample (Fig. 4(e) and (f)). The results indicate that a larger extent of continuous absorption domains are formed in the samples with increasing MW, as a result of increased conjugation and delocalization. The nanoscale absorption images probed by SNOM provide direct information about the interplay between topography and absorption density in the polymer hybrid photovoltaic device application, since both the morphology and optical absorption of photovoltaic materials usually play crucial roles in determining the power conversion efficiency. We further used high resolution AFM to study the effect of polymer MW on the nanoscale morphology of P3HT/TiO$_2$ nanorod hybrid films as shown in Fig. 5. The morphology and phase diagrams demonstrate that the rod-like structure is formed in the low MW hybrid sample while the high MW hybrid sample tends to form small nodule-like structure. The AFM data suggest that the rod-like structure of the low MW hybrid sample consists of a large amount of grain boundaries, which usually limit mobility and hinder carrier transport. In contrast, the nodule-like structure of the high MW hybrid sample shows less well-defined grain boundaries and a greater extent of continuous domains due to
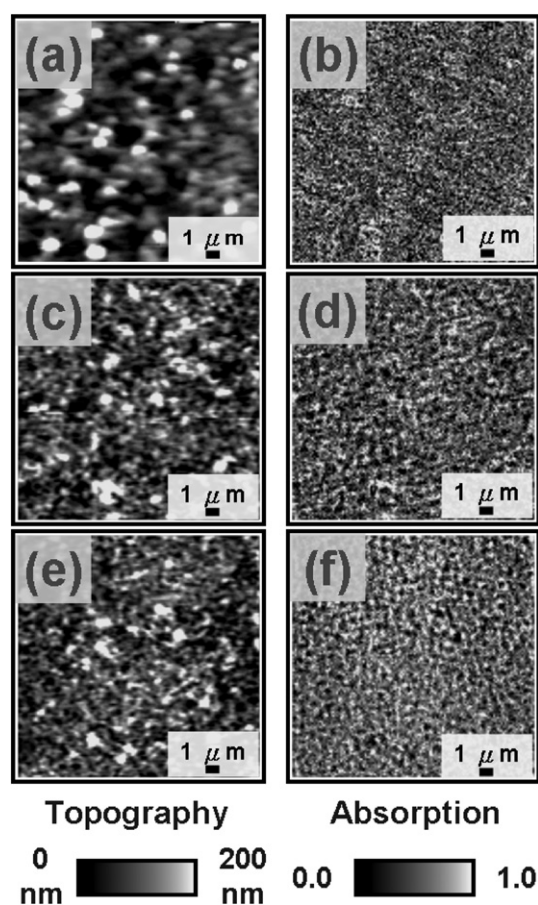

Fig. 4 Topography (a,c,e) and optical contrast images (b,d,f) of P3HT/TiO$_2$ samples with three different P3HT molecular weights obtained in SNOM transmission mode using laser radiation with 632.8 nm wavelength. The MWs in the P3HT/TiO$_2$ nanorod hybrid samples are low MW for (a,b), medium MW for (c,d) and high MW for (e,f). The scan size is 20 μm × 20 μm.

the increased conjugation as a result of enhanced polymer chain packing, which can improve the transport of charge carriers. In addition, the decrease in the number of grain boundaries and surface roughness for the P3HT/TiO$_2$ nanorod hybrid film with high polymer MW is also consistent with the observation of a more continuous absorption mapping image by SNOM measurement. In the data of the device performance in Fig. 3, the observation of an increased V_{oc} in the high MW sample might be also attributed to the decreased number of grain boundaries, which can usually act as the recombination sites for carriers. The reduction of back charge recombination may increase the position of the quasi-Fermi level and V_{oc}.[31] The nanoscale morphology of the hybrid samples with different MWs reveals the possible nature of the effect of polymer MWs on absorption, carrier transport and power conversion efficiency of P3HT/TiO$_2$ nanorod hybrid solar cells.

We also conducted confocal Raman microscopic measurements to gain insight into the component distribution of the P3HT/TiO$_2$ nanorod hybrid sample. Fig. 6(a) shows the confocal Raman image of the P3HT/TiO$_2$ nanorod hybrid with high MW. Fig. 6(b) and (c) show the corresponding Raman shift spectra resulting from the different selected areas. For comparison, the
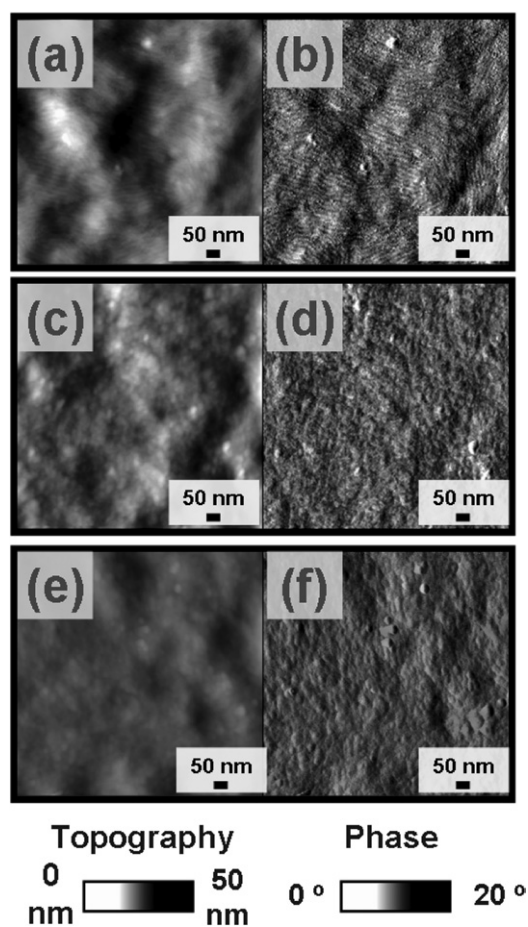
Fig. 5 Topography (a,c,e) and phase images (b,d,f) of P3HT/TiO$_2$ nanorod hybrid samples with three kinds of P3HT MWs obtained in AFM tapping mode, scan size is 2 μm × 2 μm. Images (a,b) were obtained from the low MW sample of P3HT/TiO$_2$ nanorod hybrid; (c,d) were obtained from the medium MW sample; (e,f) were obtained from the high MW sample.

Fig. 6 (a) Confocal Raman mapping image of the P3HT/TiO$_2$ nanorod hybrid sample with high MW. Images (b) and (c) show the corresponding Raman shift spectra resulting from different selected areas (regions I and II) respectively. The Raman shift spectra for TiO$_2$ and pristine P3HT are also shown in the insets of (b) and (c) respectively.

Raman shift spectra of TiO$_2$ and pristine P3HT are also shown in the insets. For TiO$_2$ nanorods, the prominent Raman peak at 516 cm^{-1} is assigned to the Ti–O stretching vibration and the peak at 639 cm^{-1} is assigned to the E$_g$ mode for anatase TiO$_2$.[32] For pristine P3HT, the prominent Raman bands at 1440 and 1380 cm^{-1} result from the C=C stretching vibrations of the thiophene ring and C–C skeletal stretching respectively.[33] The peak at 728 cm^{-1} is assigned to the deformation vibration of the C–S–C bonds. From the Raman mapping image, region I represents a TiO$_2$ rich region with strong TiO$_2$ vibrational signatures and region II represents a P3HT rich region with predominant P3HT vibrational signatures. No large extent of phase segregation as reported in the P3HT/PCBM hybrid[34] was found in our P3HT/TiO$_2$ nanorod hybrid sample, which may result from the less mobile nature of TiO$_2$ nanorods compared to PCBM molecules.

4. Conclusion

In conclusion, we have performed the nanoscale investigation of the effect of polymer MW on the performance of photovoltaic dev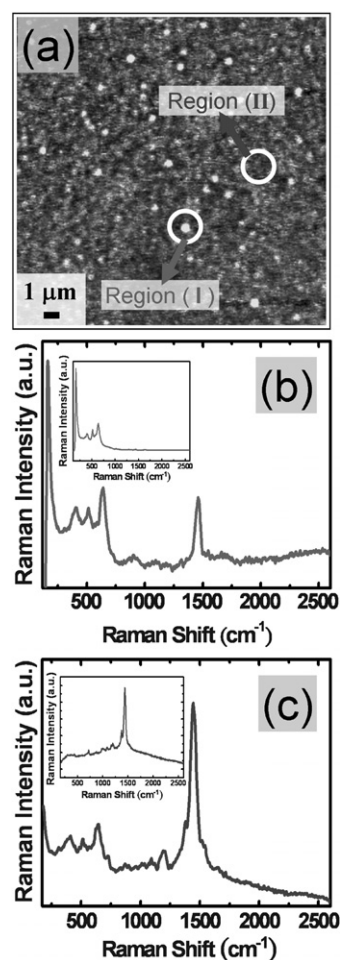ices based on P3HT/TiO$_2$ nanorod hybrid materials. From the data measured by SNOM and AFM, a more continuous absorption region and a reduction in the number of grain boundaries for the high MW P3HT/TiO$_2$ nanorod hybrid film can be obtained due to enhanced electronic delocalization. The confocal Raman mapping images also provide information for the component distribution in the hybrids. The results provide a direct observation of the correlation between the nanoscale absorption, morphology and device performance in P3HT/TiO$_2$ nanorod hybrid solar cells.

Acknowledgements

References

1 W. U. Huynh, J. J. Dittmer and A. P. Alivisatos, *Science*, 2002, **295**, 2425.
2 W. Ma, C. Yang, X. Gong, K. Lee and A. J. Heeger, *Adv. Funct. Mater.*, 2005, **15**, 1617.

3 G. Li, V. Shrotriya, J. Huang, Y. Yao, T. Moriarty, K. Emery and Y. Yang, *Nat. Mater.*, 2005, **4**, 864.
4 R. H. Friend, G. J. Denton, J. J. M. Halls, N. T. Harrison, A. B. Holmes, A. Kohler, A. Lux, S. C. Moratti, K. Pichler, N. Tessler, K. Towns and H. F. Wittmann, *Solid State Commun.*, 1997, **102**, 249.
5 T. J. Savenije, J. M. Warman and A. Goossens, *Chem. Phys. Lett.*, 1998, **287**, 148.
6 A. C. Arango, L. R. Johnson, V. N. Bliznyuk, Z. Schlesinger, S. A. Carter and H. H. Horhold, *Adv. Mater.*, 2000, **12**, 1689.
7 M. Granström, K. Petritsch, A. C. Arias, A. Lux, M. R. Andersson and R. H. Friend, *Nature*, 1998, **395**, 257.
8 W. J. E. Beek, M. M. Wienk, M. Kemerink, X. Yang and R. A. J. Janssen, *J. Phys. Chem. B*, 2005, **109**, 9505.
9 Y. Y. Lin, T. H. Chu, C. W. Chen, W. F. Su, C. C. Lin, C.-H. Ku, J. J. Wu and C. H. Chen, *J. Mater. Chem.*, 2007, **17**, 4571.
10 T. W. Zeng, Y. Y. Lin, H. H. Lo, C. W. Chen, C. H. Chen, S. C. Liou, H. Y. Huang and W. F. Su, *Nanotechnology*, 2006, **15**, 5387.
11 J. Boucle, R. Ravirajan and J. Nelson, *J. Mater. Chem.*, 2007, **11**, 3141.
12 K. M. Coakley and M. D. McGehee, *Appl. Phys. Lett.*, 2003, **83**, 3380.
13 Q. Fan, B. McQuillin, D. D. C. Bradley, S. Whitelegg and A. B. Seddon, *Chem. Phys. Lett.*, 2000, **347**, 325.
14 H. Wang, C. C. Oey, A. B. Djurisic, K. K. Y. Man, W. K. Chan, M. H. Xie, Y. H. Leung, P. C. Chui, A. Pandey and J. M. Nunzi, *Appl. Phys. Lett.*, 2005, **87**, 023507.
15 Y. T. Lin, T. W. Zeng, W. Z. Lai, C. W. Chen, Y. Y. Lin, Y. S. Chang and W. F. Su, *Nanotechnology*, 2006, **17**, 5781.
16 T. W. Zeng, Y. Y. Lin, C. W. Chen, W. F. Su, C. H. Chen, S. C. Liou and H. Y. Huang, *Nanotechnology*, 2006, **17**, 5387.
17 P. A. Van Hal, M. M. Wienk, J. M. Kroon, W. J. Verhees, L. H. Sloof, W. J. H. Van Gennip, P. Jonkheijm and R. A. J. Janssen, *Adv. Mater.*, 2003, **15**, 118.
18 Q. Qiao and J. T. McLeskey, *Appl. Phys. Lett.*, 2005, **86**, 153501.
19 R. J. Kline, M. D. McGehee, E. N. Kadnikova, J. Liu and J. M. J. Fréchet, *Adv. Mater.*, 2003, **15**, 1519.
20 C. Goh, R. J. Kline and M. D. McGehee, *Appl. Phys. Lett.*, 2005, **86**, 122110.
21 A. Zen, J. Pflaum, S. Hirschmann, W. Zhuang, F. Jaiser, U. Asawpirom, J. P. Rabe, U. Scherf and D. Neher, *Adv. Funct. Mater.*, 2004, **14**, 757.
22 W. Ma, J. Y. Kim, K. Lee and A. J. Heeger, *Macromol. Rapid Commun.*, 2007, **428**, 1776.
23 A. Cadby, R. Dean, A. M. Fox, R. A. L. Jones and D. G. Lidzey, *Nano Lett.*, 2005, **5**, 2232.
24 A. Cadby, R. Dean, R. A. L. Jones and D. G. Lidzey, *Adv. Mater.*, 2007, **18**, 742.
25 E. Klimov, W. Li, X. Yang, G. G. Hoffmann and J. Loos, *Macromolecules*, 2006, **39**, 4493.
26 C. R. McNeill, H. Frohne, J. L. Holdsworth and P. C. Dastoor, *Nano Lett.*, 2004, **4**, 2503.
27 H. Aoki, M. Anryu and S. Ito, *Polymer*, 2005, **46**, 5896.
28 R. S. Loewe, S. M. Khersonsky and R. D. McCullough, *Adv. Mater.*, 1999, **11**, 250.
29 P. D. Cozzoli, A. Kornowski and H. Weller, *J. Am. Chem. Soc.*, 2003, **125**, 14539.
30 W. J. E. Beek, M. M. Wienk and R. A. J. Janssen, *Adv. Funct. Mater.*, 2006, **16**, 1112.
31 H. J. Snaith, A. J. Moule, C. Klein, K. Meerholz, R. H. Friend and M. Graetzel, *Nano Lett.*, 2007, **7**, 3372.
32 T. Ohsaka, F. Izumi and Y. Fujiki, *J. Raman Spectrosc.*, 1978, **7**, 321.
33 M. Baibarac, M. Lapkowski, A. Pron, S. Lefrant and I. Baltog, *J. Raman Spectrosc.*, 1998, **29**, 825.
34 E. Klimov, W. Li, X. Yang, G. G. Hoffmann and J. Loos, *Macromolecules*, 2006, **39**, 4493.